# Validation and application of nonlinear hydrodynamics from CFD in an engineering model of a semi-submersible floating wind turbine

Haoran Li [a,*], Erin E. Bachynski-Polić [a,b]

[a] *Department of Marine Technology, Norwegian University of Science and Technology (NTNU), Trondheim, Norway*
[b] *Centre for Autonomous Marine Operations and Systems (AMOS), NTNU, Trondheim, Norway*

A B S T R A C T

Nonlinear hydrodynamics play a significant role in accurate prediction of the dynamic responses of floating wind turbines (FWTs), especially near the resonance frequencies. This study investigates the use of computational fluid dynamics (CFD) simulations to improve an engineering model (based on potential flow theory with Morison-type drag) by modifying the second-order difference-frequency quadratic transfer functions (QTFs) and frequency-dependent added mass and damping for a semi-submersible FWT. The results from the original and modified engineering models are compared to experimental data from decay tests and irregular wave tests. In general, the CFD results based on forced oscillation tests suggest increasing the frequency-depending added mass and damping at low frequencies compared to first order potential flow theory. The modified engineering model predicts natural periods close to the experimental results in decay tests (within 5%), and the underprediction of the damping is reduced compared to the original engineering model. The motions, mooring line tensions and tower-base loads in the low-frequency response to an irregular wave are underestimated using the original engineering model. The additional linear damping increases this underestimation, while the modified QTFs based on CFD simulations of a fixed floater in bichromatic waves result in larger difference-frequency wave loads. The combined modifications give improved agreement with experimental data in terms of damage equivalent loads for the mooring lines and tower base.

## 1. Introduction

One of the challenges facing the development of floating wind turbines (FWTs) is to accurately predict the global responses due to nonlinear hydrodynamic loads on the floater [1–5]. In the present work, the focus is on a semi-submersible FWT, known as "DeepCWind", which consists of four cylindrical columns linked with a set of braces, defined by Robertson et al. [6,7].

Numerous investigations [8–12] have used potential flow theory, typically combined with a Morison-type viscous drag model, to predict the hydrodynamic loads on various semi-submersible FWTs. The second-order sum- and difference-frequency wave-excitation loads have been shown to excite eigenfrequencies of semi-submersible floating systems, leading to larger low-frequency motions that strain the mooring system [9] or to structural vibrations [12]. The use of the full QTF instead of Newman's approximation is known to

---

* Corresponding author.
  *E-mail address:* haoran.li@ntnu.no (H. Li).

better simulate the dynamic responses of semi-submersible FWTs [12]. Gueydon et al. [10] concluded that the second-order difference-frequency loads have significant effects on the dynamic responses of semi-submersible FWTs, while sum-frequency loads have negligible contributions to the motions. Additionally, Xu et al. [13] found the effect of difference-frequency wave loads on the responses of FWTs was more significant as the water depth decreased. Furthermore, Luan et al. [14] illustrated the importance of the viscous drag force from Morison's equation, especially related to the excitation and damping of resonant motions. Correctly choosing the drag coefficient often requires model tests or higher fidelity numerical models.

In the present work, an approach with first and second order potential flow theory combined with Morison-type drag will be referred to as an "engineering model". In the international collaboration project known as OC5 (Phase II) [4], Robertson et al. found that engineering models severely underpredicted the low-frequency nonlinear wave loads and dynamic responses of a semi-submersible FWT because these models limit hydrodynamic modeling to linear or weakly nonlinear models. In the OC5 project [4], all of the participants who used a combination of potential flow and Morison-type drag underestimated both the extreme tower base loads and damage equivalent loads in a wave-only condition by 10–40% compared to the experimental results. The main underprediction was attributed to the responses at the pitch natural frequency. On the other hand, Wang et al. [15] and Benitz et al. [16,17] demonstrated that computational fluid dynamics (CFD) methods have the potential ability to more precisely predict nonlinear difference-frequency wave loads and capture shadowing effects and transverse forces from vortex shedding, but at a significantly higher computational cost.

In addition to the nonlinear wave loads, hydrodynamic coefficients, such as added mass or damping coefficients, also significantly affect the dynamic responses of a semi-submersible FWT when using engineering models. For example, Wei et al. [5] found the heave plates of a semi-submersible FWT provide additional added mass and enhance the flow separation and vortex shedding processes. The existence of heave plates (see the left subplot of Fig. 1) together with the interactions between columns and braces generate more stringent requirements for the fidelity of simulation tools. Compared to CFD methods, Lopez-Pavon et al. [18] and Bozonnet et al. [19] found potential flow theory did not predict the increased added mass due to the edge of heave plates and underestimated the added mass for a platform with heave plates. In addition, CFD methods found the added mass and damping were largely dependent on the motion amplitude and viscous effects were predominant in the damping term, both of which are incompatible with the assumptions of linear potential flow theory. Some studies [19–21] extracted the damping coefficients from CFD simulations of free decay motions of a semi-submersible FWT and demonstrated that CFD methods can better quantify the viscous damping characteristics.

Dynamic responses of FWTs to regular waves have been simulated and compared by the engineering models and CFD methods [22–25]. When nonlinear phenomenon were not dominant, the results obtained by the engineering models and CFD methods showed reasonable agreement, while larger discrepancies occurred for highly nonlinear regular waves.

In the current study, the difference-frequency surge force and pitch moment QTFs from second-order potential flow theory are modified based on the estimated difference-frequency wave loads on a restrained floater subjected to bichromatic waves in the CFD simulations. The frequency-dependent added mass and damping coefficients from the first-order potential flow theory are modified based on the calculated linearized added mass and damping coefficients from CFD simulations of forced oscillations around the surge, heave and pitch natural periods. The engineering tool with modified QTFs and added mass and damping coefficients is then validated against the free decay motions in surge, heave, and pitch (from both CFD simulations and experiments), and responses in irregular waves (from experiments). Furthermore, the consequences of the modifications on the estimation of short-term extreme response statistics and damage equivalent loads of mooring lines and tower base are investigated.

The organization of this paper is as follows. Section 2 describes the experimental setups. The modifications of QTFs and added mass and damping coefficients are presented in Section 3 together with the introduction of engineering model and the methodology for analyzing the results. The surge, heave and pitch decay are examined in Section 4.1, while the dynamic responses and damage equivalent loads under irregular waves are analyzed in Section 4.2. Conclusions are drawn in Section 5.

## 2. Experiment setup

In the present work, in order to validate the engineering model with modified nonlinear hydrodynamics from CFD and investigate
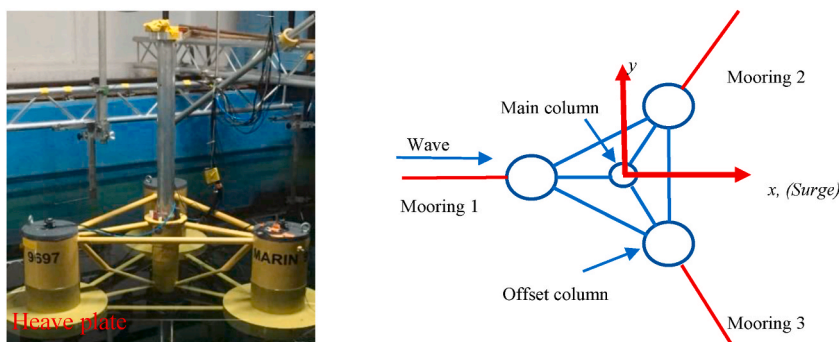


**Fig. 1.** DeepCwind semi-submersible FWT (left: Geometry of FWT [26], right: Mooring system).

the resulting dynamic responses due to nonlinear hydrodynamic loads, two sets of experimental data are considered. In Phase I of the Offshore Code Comparison Collaboration, Continued, with Correlation, and unCertainty (OC6), the semi-submersible was subjected to wave loads in a narrow towing tank. A linear mooring system was applied, and tower base loads were not measured. In Phase Π of the Offshore Code Comparison Collaboration, Continued, with Correlation (OC5) project, the same floater geometry (left subplot of Fig. 1) was tested in an ocean basin, with a catenary mooring system, and with an instrumented flexible tower. Both sets of experiments were conducted at the Maritime Research Institute Netherlands (MARIN) for the same OC5-DeepCwind semi-submersible floater [7] at 1:50 scale. A summary of floater geometry is given in Table 1. The right-handed coordinate system used here originates at the center of the floater at the still water line, with positive $y$ towards the starboard column, and $z$ upward. All data and results are given at full scale in this paper, except when explicitly mentioned.

For the configuration of OC6 project shown in the right subplot of Fig. 1, the wind turbine was removed, but the inertial properties of the floater with tower correspond to the total inertial properties of system in the OC5 Project. Considering the limitation of basin width (Table 2), the mooring system in the OC6 project consisted of 3 taut-spring-lines to reproduce the equivalent linear stiffness of the catenary system in the OC5 project. Robertson et al. [7,26] provide the dimensions and structural properties of the system in the OC5 and OC6 projects. The global motions, such as surge ($x$-displacement), heave ($z$-displacement) and pitch ($y$-rotation), the mooring line tensions, and tower base loads were measured. Table 2 also compares the water depth and the parameters of the selected irregular wave following the JONSWAP wave spectrum in the OC5 and OC6 projects which are nearly identical.

## 3. Methodology

The CFD simulations to estimate the difference-frequency QTFs (section 3.2) and frequency-dependent added mass and damping (section 3.3) were performed with the open-source CFD toolbox OpenFoam [27] where the two-phase incompressible Navier-Stokes equations were solved. The Volume-Of-Fluid method [28] was used to capture the free surface and a six-degree of freedom solver was coupled to solved the flow-dependent motions [22]. The $k - \omega$ SST turbulence model was applied. See previous works [29,30] for additional details.

### 3.1. Time-domain analysis

The time-domain analysis is performed using the engineering model SIMA (SIMO-RIFLEX) [31,32] which is developed by SINTEF Ocean. The floater and the rotor-nacelle-assembly (RNA) are modelled as rigid bodies, while the mooring lines and tower are represented as nonlinear bar or beam elements, respectively. The first-order wave-excitation forces and second-order sum-frequency wave forces on the floater are estimated based on the potential flow theory [33]. However, the added mass, damping and second-order difference-frequency wave forces are modified based on the CFD simulations. In addition, viscous effects are considered by applying drag forces of Morison's equation to the columns and cross braces. A constant drag coefficient in the normal direction (0.774, based on towing tests [26]) is applied for each part of the floater and a drag coefficient in the axial direction (2.48, based on previous comparisons of a similar engineering tool with experimental data from the DeepCwind test campaign [6]) is applied for the heave plates of the floater.

The added mass and damping are applied as radiation forces in time domain using the convolution technique [34], and the motions of the floater can be represented as:

$$[\mathbf{M} + \mathbf{A}(\infty)]\ddot{\mathbf{x}}(t) + \int_{-\infty}^{\infty} K(t - \tau)\dot{\mathbf{x}}(\tau)d\tau + \mathbf{C}\mathbf{x}(t) = \mathbf{F}^{(1)} + \mathbf{F}^{(2)} + \mathbf{F}^{(D)} + \mathbf{F}^{(R)} \tag{1}$$

where $M$ is the mass of the floater, $A(\infty)$ is the infinite-frequency added mass, $\ddot{x}, \dot{x},$ and $\mathbf{x}$ are the acceleration, velocity and displacement of the floater, respectively. $K(t - \tau)$ is the retardation function which represents the fluid memory and is calculated from the frequency-dependent damping. $\mathbf{C}$ is the hydrostatic restoring, $\mathbf{F}^{(1)}$ is the first-order wave excitation force, $\mathbf{F}^{(2)}$ is the second-order mean, rapidly varying and slowly varying wave drift force, $\mathbf{F}^{(D)}$ is Morison drag force and $\mathbf{F}^{(R)}$ are the forces from RIFLEX elements, such as mooring lines and tower.

Different combinations of modifications based on CFD are considered in the SIMA simulations, ranging from none (SIMA-W) to all (SIMA-C), as summarized in Table 3. All SIMA models include automatically added linear damping to ensure that cutting-off the retardation function does not result in negative damping. In addition, extra linear damping (Table 3) which is determined by matching the calculated free decay motions of the floater from the CFD simulations is included in SIMA-WL. When comparing with experimental

**Table 1**
OC5-DeepCwind semi-submersible floater geometry.

| | |
|---|---|
| Total draft | 20.0 m |
| Diameter of main column | 6.5 m |
| Diameter of offset (upper) column | 12.0 m |
| Diameter of heave plate | 24.0 m |
| Center-center distance between two offset columns | 50.0 m |

**Table 2**
Water depth, basin width and irregular wave conditions from the OC5 and OC6 projects.

|  | OC5 project | OC6 project |
| --- | --- | --- |
| Water depth (m) | 200.0 | 180.0 |
| Basin width (m) | 36.0 | 4.0 |
| Significant wave height (m) | 7.1 | 7.4 |
| Peak period (s) | 12.1 | 12.0 |
| Peak enhancement factor (−) | 2.2 | 3.3 |

results, for all SIMA models, the wave is obtained by filtering the experimentally measured wave elevation at the origin by a high-pass filter with a 0.005 Hz cut-off frequency. All irregular wave components are treated as linear, and assumed to travel in the positive $x$-direction. In addition, a series of irregular waves with significant wave height $H_s = 7.1$ m, peak period $T_p = 12.1$ s and different wave seeds are selected to predict the short-term extreme values. These irregular waves are generated in SIMA based on the JONSWAP spectrum with the peak enhancement factor equal to 3.3.

### 3.2. Hydrodynamic added mass and damping with CFD simulations

To estimate the hydrodynamic added mass and damping near the resonance frequencies, several forced oscillations around the surge, heave and pitch natural periods were performed using CFD model [29]. The first harmonic component of the hydrodynamic wave load was extracted and decomposed into in-phase and out-of-phase components to find the added mass and linearized damping. The pitch moment from forced oscillations in surge and the surge force from forced oscillations in pitch are used to calculate cross terms (pitch-surge/surge-pitch).

The first-order radiation solution is used to calculate the added mass and damping in potential flow theory. However, the assumption of inviscid flow requires the potential flow solutions to be augmented with viscous effects by including Morison-type drag. In WAMIT [33], the results include the frequency-dependent added mass and damping from the columns, the frequency-independent added mass of the braces calculated by applying the inertial term of Morison's equation (the added mass coefficient is 1.0) and linearized damping of the columns and braces obtained from the drag term of Morison's equation applying the Fourier-averaged approach.

Because Morison drag forces on the columns and braces are calculated separately in the time domain analysis, the linearized damping from Morison-type drag should be deducted from the damping of CFD simulations when modifying the damping from WAMIT. The added mass and damping near the resonance frequencies are replaced with CFD results. To obtain coefficients for frequencies without CFD results available, for the regions below the resonance frequencies, the gradient remains constant. When the frequency is larger than the resonance frequencies, the gradient varies to ensure a smooth transition from CFD results to WAMIT results (dashed line in Fig. 2). Because the pitch-surge results are equal to the surge-pitch results, only surge (11), heave (33), pitch (55) and pitch-surge (51) added mass (A) and damping (B) are presented in Fig. 2. The other terms are calculated in WAMIT and not shown in this paper. In SIMA, the retardation function is obtained based on the modified frequency-dependent damping. The infinite-frequency added mass is then modified to give the best match between the added mass calculated from the retardation function and the input (modified) frequency-dependent added mass.

The results in Fig. 2 show that the potential flow theory underestimates the amplitude of the added mass at low frequencies by over 10%. A possible explanation is that flow separation and the formation of eddies at the edge of the heave plates change the phase of the pressure relative to the floater motion. Based on the comparisons of damping, the quadratic damping from Morison drag force underestimates the nonlinear viscous damping. The difference depends on the selected drag coefficient (See Sec. 3.1).

### 3.3. Difference-frequency quadratic transfer functions with CFD simulations

In previous work, CFD simulations were used to calculate the difference-frequency wave loads on a restrained semi-submersible FWT subjected to 24 pairs of bichromatic waves [30]. The bichromatic waves were generated by adding together two regular waves with different wave frequencies. The first order components of bichromatic waves were close to the peak periods of the irregular wave while the difference frequency aligned with either the surge or pitch natural frequency of the FWT where the largest wave-induced responses can be excited in irregular waves [35]. The wave amplitudes (around 1.75 m) of wave component were determined by making the calculated maximum wave height when two waves are added linearly close to the wave height of the

**Table 3**
Overview of different settings for time-domain simulations in SIMA.

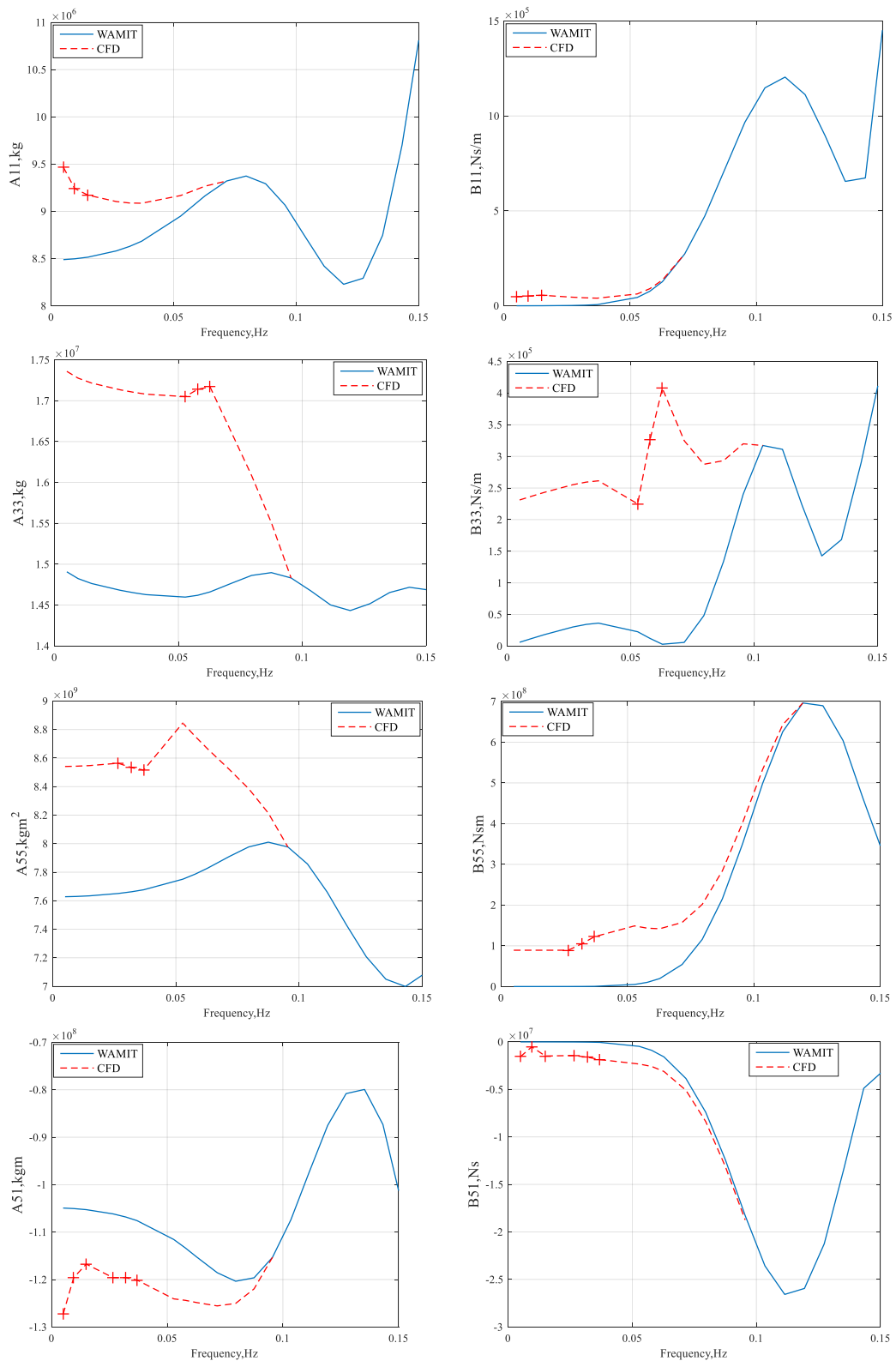| Label | Difference-frequency QTF | Added mass and damping | Additional linear damping |
| --- | --- | --- | --- |
| SIMA-W | Potential flow theory | Potential flow theory | x |
| SIMA-WL | Potential flow theory | Potential flow theory | √ |
| SIMA-CA | Potential flow theory | CFD (forced oscillations) | x |
| SIMA-CQ | CFD (bichromatic waves) | Potential flow theory | x |
| SIMA-C | CFD (bichromatic waves) | CFD (forced oscillations) | x |

**Fig. 2.** Comparisons of the added mass and damping between CFD and WAMIT ("+" represents the CFD results from forced oscillation simulations).

irregular-wave (7.1 m) [35]. However, wave amplitudes decreased for shorter wave periods due to the occurrence of significant wave damping in the CFD simulations. The amplitudes and phases of difference-frequency wave loads and each harmonic component of the bichromatic waves were calculated by fitting a second order expansion model to the steady-state part of the numerical time signal with a least squares procedure. Then the values of the QTFs for each of the 24 frequency combinations were calculated by comparing the amplitudes and phases between difference-frequency wave loads and incident waves.

The second-order potential flow theory approximates the nonlinear free-surface boundary condition and wave-body interaction, including the quadratic interaction of first-order quantities. Hence, the second-order wave loads are computed by sum of quadratic contributions from the first-order solution, as well as contributions given by the solution of the second-order velocity potential. See Pinkster [36] for details. WAMIT [33] can completely calculate the second-order velocity potential by including the contributions of incoming wave, diffracted and radiated wave and is used in the current research.

In the CFD simulations, the floater was restrained. The QTFs for the fixed condition ($QTF_{CFD,fixed}$) were estimated by subtracting the contributions of the Morison drag and the difference-frequency wave components. However, the contributions due to the first-order motions were not included in the CFD results. Because the first-order motion is predicted well by the first-order potential flow solution, it is assumed that the contribution due to the first-order motion can be accurately estimated by the difference of QTFs for the fixed and floating floater in WAMIT. Hence, the QTF values based on CFD simulations for the floating condition are expressed as:

$$QTF_{CFD,floating} = QTF_{CFD,fixed} + \left( QTF_{WAMIT,floating} - QTF_{WAMIT,fixed} \right). \tag{2}$$

Taking advantage of symmetry relations, we consider the upper-left-half ($f_2 \geq f_1$ in the left subplot of Fig. 3) when discussing how the QTF from potential flow is modified. The diagonal of the difference-frequency QTF matrix ($f_2 = f_1$) represents the mean drift force, which only depends on first order information and is not modified. The amplitudes and phases of QTFs from WAMIT along the surge and pitch natural frequencies are replaced with the available results from CFD simulations. To propagate the correction to other parts of the QTFs, the WAMIT magnitudes or phases with the same $f_2$ are extracted and corrected based on the results from CFD model. There are two different cases: in case (1), regions with only one value from CFD model, the gradient is maintained to be the same before and after modification; in case (2), regions with two values from CFD model or one value from CFD and one value from WAMIT, the gradient varies linearly between CFD values or CFD and WAMIT values. An example is shown in the right subplot of Fig. 3. The modified QTF is referred to as 'New QTF'. 'Old QTF' is the QTF estimated in WAMIT. Additional details regarding the bichromatic wave simulations and modification procedure for the fixed structure can be found in the previous publication [30].

The magnitudes and phases of the old and new surge force QTF for the floating semi-submersible are presented in Fig. 4. Close to the surge natural frequency, the magnitudes of the new QTF are close to the magnitudes of the old QTF for lower wave frequencies (0.05–0.09 Hz). At higher wave frequencies, the new QTF has higher magnitudes, especially around the pitch natural frequency. The phases of the new QTF follow a similar patten as the old QTF, but differ in value.

The new and old pitch moment QTFs are compared in Fig. 5. Compared to the QTF from potential flow theory, the new magnitudes have similar pattern and values except for the larger moments at the higher wave frequencies. The phase of the new QTF is similar to the old QTF, but big differences occur at the lower wave frequencies between surge and pitch natural frequency.

### 3.4. Damage equivalent loads

Engineering global analysis models can be used to obtain time series of loads in certain FWT components, such as the tower or mooring lines [37,38]. When comparing against experimental results in irregular waves, the damage equivalent loads can provide a useful metric for comparing results. For a given time series of loads from experiments or simulations, the total damage ($D$) can be determined based on Miner's rule by linearly accumulating the damage from each stress or tension level:
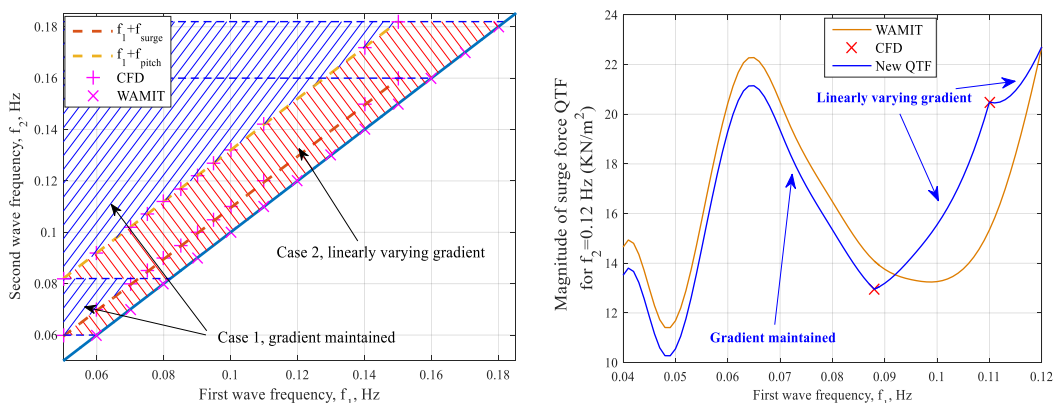


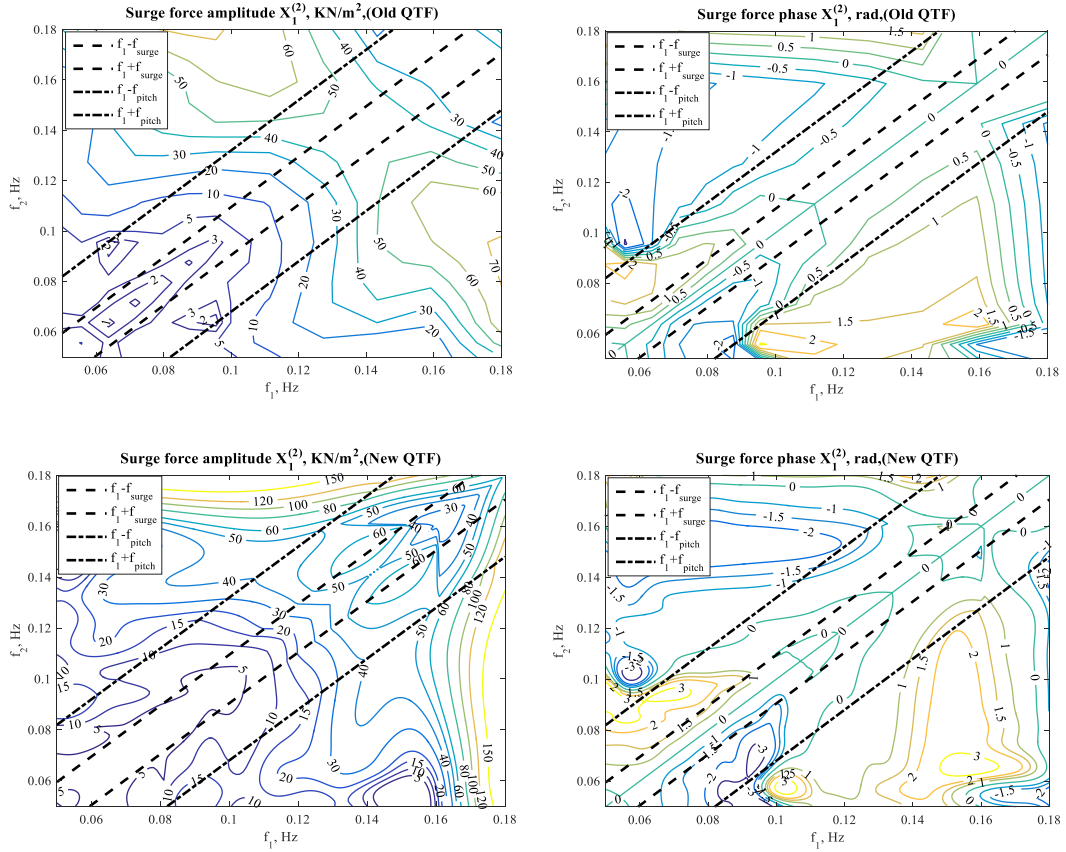**Fig. 3.** Different regions of the QTF for modification.

**Fig. 4.** Magnitudes and phases of surge force QTF.

$$D = \sum_i \frac{n_i}{N_i} \tag{3}$$

where $n_i$ is the number of cycles at the $i$th stress or tension range in the time series and $N_i$ is the number of cycles to failure at the same stress or tension range according to the S–N curve. In the present work, damage equivalent loads, calculated using a Matlab-based tool (MLife [39]) are used as a metric to quantify the damage. The S–N curve is given as

$$N_i = \left( \frac{\sigma^{ult} - |\sigma^{MF}|}{1/2\sigma_i} \right)^m \tag{4}$$

where $\sigma_i$ is the $i$th stress or tension range. $\sigma^{ult}$ is the ultimate design stress or tension of the material, $\sigma^{MF}$ is the fixed mean stress or tension value in the time series and $m$ is the Wöhler exponent. The rainflow counting method [40] is applied to count the cycles. The damage equivalent load $\sigma^E$ is a constant-amplitude damage-load at a fixed frequency that produces equivalent damage as the variable loads.

$$D = \frac{n^E}{N^E} \tag{5}$$

$$n^E = f^E \cdot T \tag{6}$$

$$N^E = \left( \frac{\sigma^{ult} - |\sigma^{MF}|}{1/2\sigma^E} \right)^m \tag{7}$$

where $n^E$ is the total equivalent damage counts in the time series, $f^E$ is the frequency of the damage equivalent load, $T$ is the elapsed time of time series and $\sigma^E$ is found by forcing Eq. (5) to be equal to Eq. (3).

The damage equivalent load of mooring line is estimated based on the tension and the damage equivalent load at the tower base is calculated based on the axial stress. The frequency $f^E$ is taken as 1 Hz and a Wöhler exponent $m = 3$ is used. The tower base coordinate system is illustrated in Fig. 6. Since the wave propagates along $x$-axis in this paper, it is sufficient to take the point B as an example for
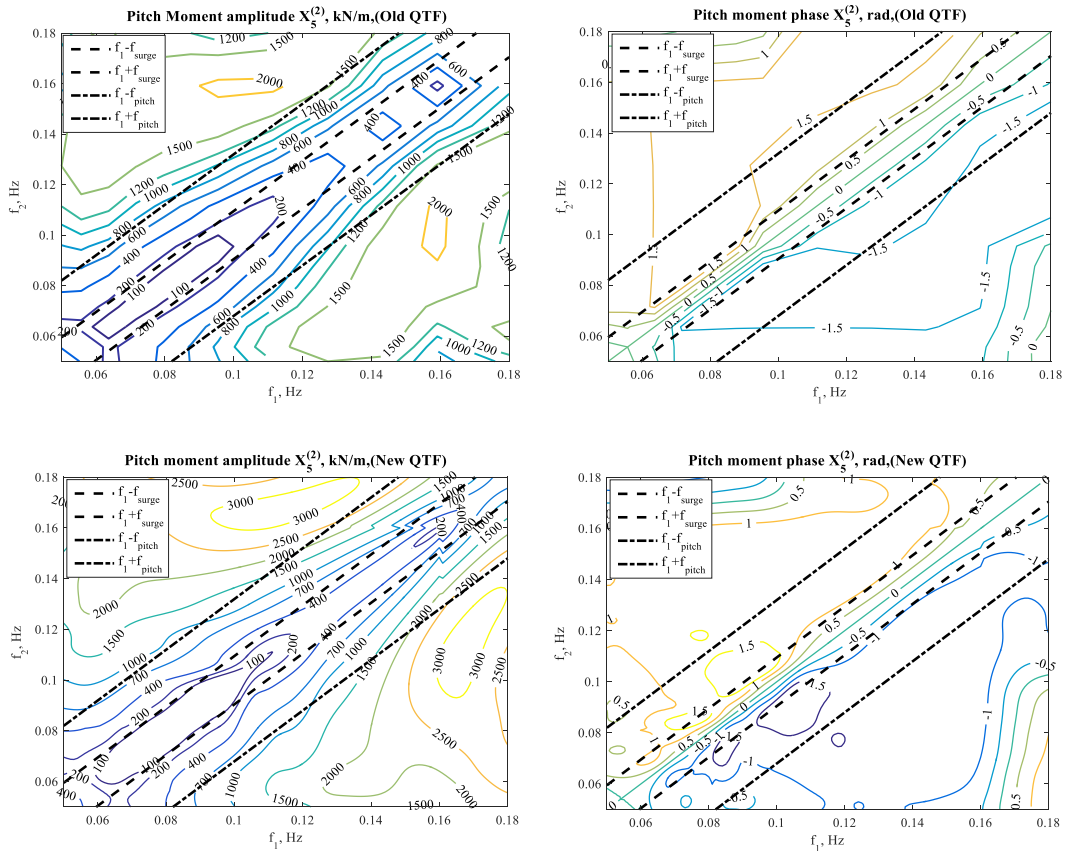
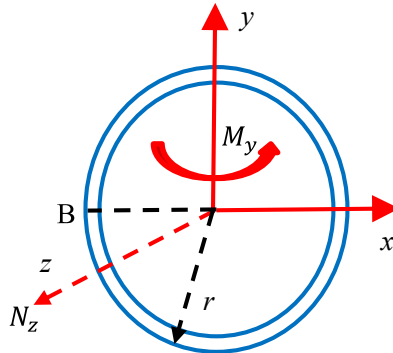**Fig. 5.** Magnitudes and phases of pitch moment QTF.



**Fig. 6.** Coordinate system of tower base (top view).

the damage analysis. Ignoring the cross-section deformation after the loads are exerted, the axial stress is equal to the nominal axial stress:

$$\sigma_B = \frac{N_z}{A} + \frac{M_y \cdot r}{I_y} \tag{8}$$

where $N_z$ is the axial force, $A$ is the nominal cross-sectional area, $M_y$, $I_y$ are the moments and sectional moments of the area about the local $y$-axis, respectively, and $r$ is the cross section radius.

### 3.5. Short-term extreme value prediction

The extreme value of a random stochastic process $X(t)$ within a given time duration is defined as the maximum value from a sequence of individual local maxima and minima.

$$X_e = \max\{X_{\max 1}, X_{\max 2}, ..., X_{\max n}, |X_{\min 1}|, |X_{\min 2}|, ..., |X_{\min n}|\} \tag{9}$$

where $X_e$ represents the extreme value and $X_{maxi}, X_{mini}$ are the individual local maxima and minima, respectively. Based on the assumption that all individual local maxima and minima are independent and identically distributed with a common distribution function $F_X(x)$, the distribution of $X_e$ can be expressed as:

$$F_{X_e}(x) = \text{Prob}\{X_e \le x\} = [F_X(x)]^{2n} \tag{10}$$

When the number of samples $2n$ is large enough, the extreme value distribution (Eq. (10)) will converge towards one of three types of distributions: Gumbel, Fréchet and Weibull distributions. Among them, the Gumbel distribution is the most recommended model for marine structures subjected to wave loads [41] and implemented in the current research. The cumulative distribution probability $F_{X_e}$ can be written as:

$$F_{X_e} = \exp(-\exp(-\alpha(x-\mu))) \tag{11}$$

where $\alpha$ is the scale parameter and $\mu$ is the location parameter.

## 4. Results and discussions

In this section, the results of the dynamic simulations are presented and discussed for free decay tests and freely floating motions under the irregular waves. The variations in the SIMA model are used to separate the effects of the modifications of the difference-frequency QTFs and added mass and damping.

### 4.1. Free decay tests

Free decay tests in still water are carried out to establish the natural periods and damping of the rigid body modes of motions. Free decay tests in surge, heave and pitch (Table 1) were carried out experimentally in the OC6 project and using all variations of the engineering model (Table 3) as well as CFD [29].

Damped natural periods are determined as the mean duration between two consecutive peaks or troughs of motion. Damping values are presented as a function of the amplitude of motion. The damping ratio ($\xi^*$) relative to the critical damping is calculated based on the logarithmic decrement ($\delta$) for each cycle:

$$\delta = \ln \frac{x_n}{x_{n+1}} \tag{12}$$

where $x_n$ and $x_{n+1}$ are two consecutive peaks or troughs. The damping ratio is then computed as:

$$\zeta^* = \frac{1}{\sqrt{1 + \left(\frac{2\pi}{\delta}\right)^2}} \tag{13}$$
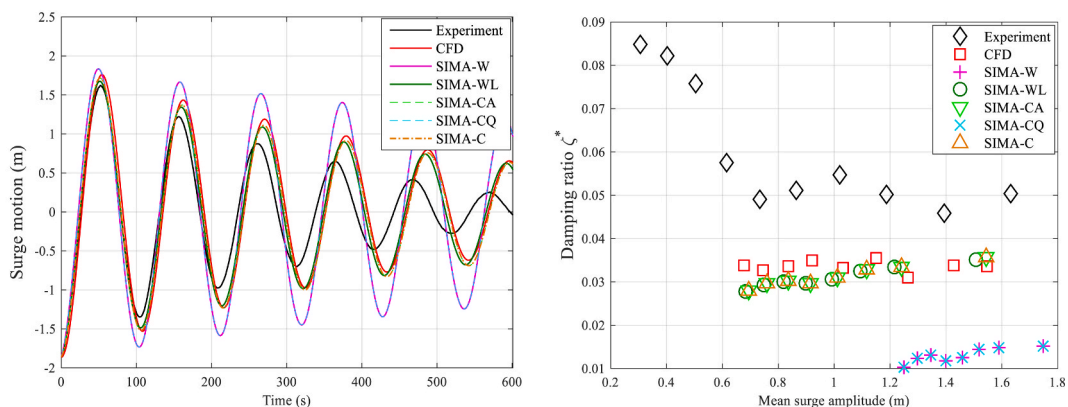


**Fig. 7.** Surge decay (left: decaying surge motion, right: surge damping ratio).

Both linear (given by the intercept) and quadratic (given by the slope) damping coefficients of the FWT can be estimated in this way. However, in some cases, especially for small motion amplitudes, there are large variations in the damping level.

### 4.1.1. Surge decay

The surge decay motions are compared in Fig. 7. All numerical models underestimate the damping compared to the experiment. However, the underestimation in the damping ratio in the CFD model is around 30%, while the original potential flow theory model (SIMA-W) underpredicts by approximately 70%. The upturning tail at small surge amplitudes in the experiment is likely due to mechanical friction [26]. This friction leads to a constant Coulomb-friction-type damping. In addition, the hydrodynamic linear damping (given by the intercept) dominates over the quadratic (given by the slope) in the experiment and all numerical models.

The modified difference-frequency surge force QTF has no effect on the free-decay surge motion (SIMA-W vs. SIMA-CQ, or SIMA-CA vs. SIMA-C). When the modified damping is used, the predicted damping in the engineering tool (SIMA-CA, SIMA-C) increases sharply and is quite close to the results in the CFD model. Similarly, after adding additional linear damping, SIMA-WL also shows similar damping as the CFD model.

All numerical models overestimate the surge natural period by around 4% compared to the experiment, as shown in Table 4. One possible reason is related to the uncertainty of mooring stiffness (about 10%) in the experiment [42] which reduces the surge natural period to around 105 s based on the analytical solution. However, the mooring stiffness has little influence on the damping [43]. The larger added mass in the modified model slightly increases the natural period (SIMA-W vs. SIMA-CA), as does the increased linear damping (SIMA-W vs SIMA-WL), but these effects are minor.

### 4.1.2. Heave decay

Fig. 8 shows the free decay in heave. The difference-frequency heave force QTF is not modified in the current research, only the added mass and damping are adjusted in SIMA-C. The motion amplitudes between experiment and all numerical models are in close proximity of each other, except the original potential flow theory model (SIMA-W). Compared to the experiment, the CFD model captures more linear damping (given by the intercept) and less quadratic damping (given by the slope). The original potential flow theory model (SIMA-W) severely underestimates the damping compared to the experiment and CFD model. However, due to the implementation of Morison-type drag, SIMA-W has similar quadratic damping (given by the slope) as the CFD model, and the difference between them comes from the linear damping. Hence, when adding linear damping, SIMA-WL captures similar damping as the CFD model. Because the frequency-dependent damping is modified based on the calculated linearized damping in the CFD simulations, the predicted damping in SIMA-C is close to the result in SIMA-WL.

Despite the difference in damping, all numerical models agree well with the experiment regarding the heave natural period (within 0.81%) as presented in Table 4.

### 4.1.3. Pitch decay

For the pitch decay, interaction between pitch and surge motions was observed in the experimental measurement due to the initial condition in the decay test. No such interaction was found in the CFD simulation. Hence, motions at the surge natural frequency are removed from the experimental signal by a high-pass filter with a 0.015 Hz cut-off frequency. The filtered experimental pitch motion is presented in Fig. 9 together with the results in all numerical models. All numerical models capture the damping well except for the underestimation in the SIMA-W and SIMA-CQ. Linear damping dominates the pitch damping, although the overall damping level in the experiment shows large variations.

As for the surge decay motion, the modified difference-frequency pitch moment QTF has no effect on the free-decay. When the modified damping (SIMA-CA, SIMA-C) or the added linear damping (SIMA-WL) is implemented, the predicted damping ratio in the engineering tools increases by around 75%.

Compared to the experiment, all numerical models slightly underpredict the pitch natural periods by up to 2.01% (Table 4). As in the analysis of the surge and heave natural periods, the larger added mass and damping in the CFD and modified SIMA models (SIMA-WL, SIMA-CA and SIMA-C) increase the pitch natural period, but the influence is quite small.

In conclusion, through modifying the added mass and damping based on the forced oscillations in CFD simulations, the engineering tools can capture similar damping as the CFD model in the free decay. Despite the difference in added mass and damping, the differences of predicted natural periods among the experiments and all numerical models are quite small.

**Table 4**
Natural periods obtained from experiments and numerical simulations.

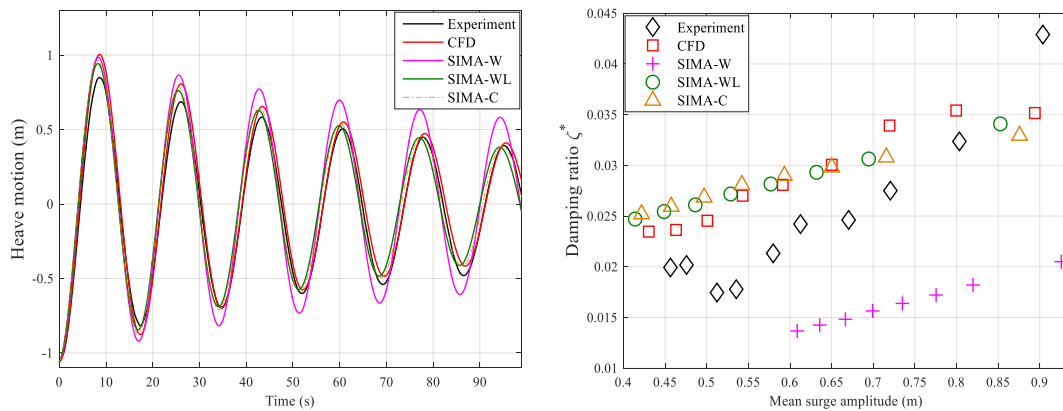|  | Surge (s) | Difference (%) | Heave (s) | Difference (%) | Pitch (s) | Difference (%) |
|---|---|---|---|---|---|---|
| Experiment | 104.1 | 0 | 17.32 | 0 | 31.29 | 0 |
| CFD | 108.4 | 4.13 | 17.39 | 0.40 | 31.07 | 0.70 |
| SIMA-W | 108.1 | 3.84 | 17.18 | 0.81 | 30.66 | 2.01 |
| SIMA-WL | 108.2 | 3.94 | 17.19 | 0.75 | 30.67 | 1.98 |
| SIMA-CA | 109.1 | 4.80 | N/A | N/A | 30.96 | 1.05 |
| SIMA-CQ | 108.1 | 3.84 | N/A | N/A | 30.66 | 2.01 |
| SIMA-C | 109.1 | 4.80 | 17.33 | 0.058 | 30.96 | 1.05 |

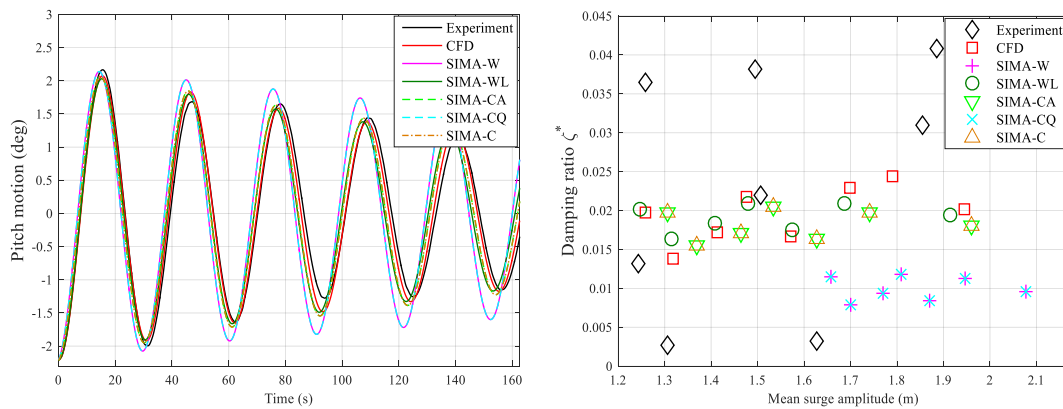**Fig. 8.** Heave decay (left: decaying heave motion, right: heave damping ratio).



**Fig. 9.** Pitch decay (left: decaying pitch motion, Experiment: high-pass filtered results, right: pitch damping ratio).

### 4.2. Irregular wave cases

In order to assess the performance of the engineering model with modified hydrodynamics based on CFD simulations, numerical results in irregular waves are compared against experimental measurements (Table 2). All SIMA simulations are carried out for at least 12,600 s and the transient phase during the first 1800 s is eliminated to obtain a 3-h simulation. A response metric (referred to as 'PSD sum' [26]) is adopted to measure the dynamic responses both within and outside the wave frequency range. The power-spectral density (PSD) sum is an integration of the one-sided, discrete power density functions of the response in the frequency range of interest. The frequency ranges are shown in Table 5. These are determined based on the ranges over which the wave spectra were defined and natural frequencies in surge, pitch and heave motions.

The numerically calculated irregular waves in all SIMA models are compared to the experimentally measured irregular waves in the OC6 project in Fig. 10 and Table 6. There is good agreement between the numerical model and experiment except for small differences in the distribution of the largest wave elevations (>6 m) and the mean value. The PSD sums in low-frequency ranges are less than 1% of the energy from the wave frequency range.

Only one realization was generated in the experiment. Meanwhile, 20 different random seeds of irregular waves were simulated numerically. The corresponding probability distribution for the 3-h maximum wave elevation based on these 20 numerical simulations is shown in Fig. 11. Most simulations have similar maximum wave elevation ranging from 7 m to 7.5 m, while two of them predict larger maxima.

**Table 5**
Frequency limits for PSD sum.

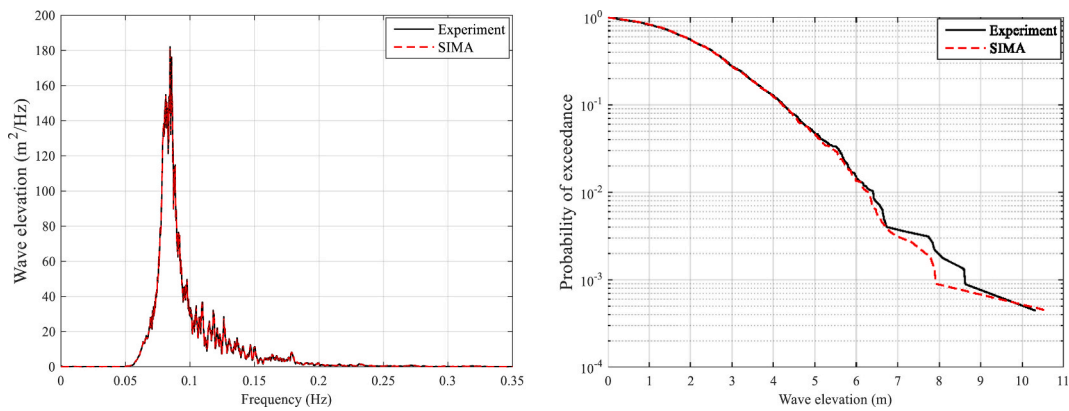|  | The lowest frequency (Hz) | The highest frequency (Hz) |
| --- | --- | --- |
| Surge natural frequency | 0.006 | 0.012 |
| Pitch natural frequency | 0.029 | 0.035 |
| Heave natural frequency | 0.054 | 0.060 |
| Wave frequency | 0.072 | 0.092 |

**Fig. 10.** Irregular wave in the OC6 project (left: PSD, right: probability of exceedance of all local maxima and minima).

**Table 6**
Statistical results and PSD sums for irregular wave elevation in the OC6 project.

|  | Mean (m) | Standard deviation (m) | Wave PSD sum (m$^2$) |
| --- | --- | --- | --- |
| Experiment | −1.50E-3 | 1.908 | 2.015 |
| SIMA | 8.75E-4 | 1.907 | 2.011 |
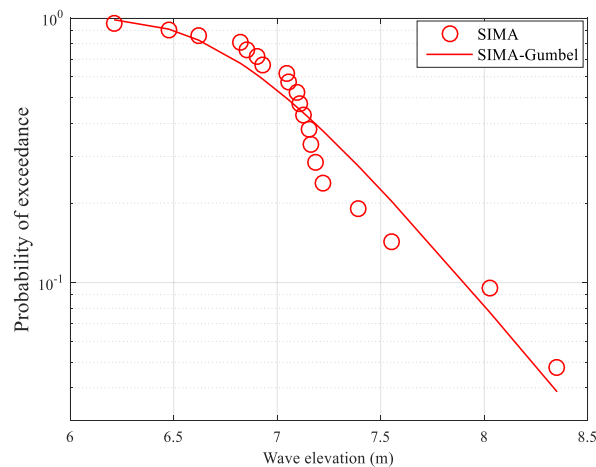


**Fig. 11.** Three-hour maximum irregular wave elevation ($H_s = 7.1\ m$, $T_p = 12.1\ s$).

### 4.2.1. Floater motions

Due to the symmetry of the model, and the fact that the waves travel along an axis of symmetry (Fig. 1), sway, roll and yaw motions are negligible. Therefore, the floater motions in surge, heave and pitch are selected as critical responses.

The numerically estimated surge motions are compared against the experimental data in Fig. 12 and Table 7. Surge resonance dominates surge motion with very little contribution from wave frequency response (Surge PSD sum vs Wave PSD sum in Table 7). Therefore, only the responses around the surge natural frequency are compared (left subplot in Fig. 11). The surge natural frequency is outside the linear wave-excitation range, and must be excited by some nonlinear force. Compared with potential flow theory, CFD can more accurately calculate the difference-frequency wave forces: the modified difference-frequency surge force QTF greatly increases the response (SIMA-CQ, SIMA-C). The maxima and standard deviation of surge motion increase by about 15% and 20% respectively in SIMA-CQ and SIMA-C. The modified frequency-dependent damping (SIMA-CA) or the additional linear damping (SIMA-WL) reduce the surge resonance. However, the effect of different low-frequency damping on the local maxima and standard deviation of surge motion is minor (SIMA-W vs SIMA-WL vs SIMA-CA). The mean value and the wave PSD sum are related to the first-order potential flow solution, and a slight difference (within 10%) is observed in all SIMA models compared to the experimental measurements. The best correspondence with the experiment is found in SIMA-C model with the modified surge force QTF and added mass and damping with CFD simulations.

Applying the modified models with numerically generated realizations of the same sea state results in the 3-h maxima distribution
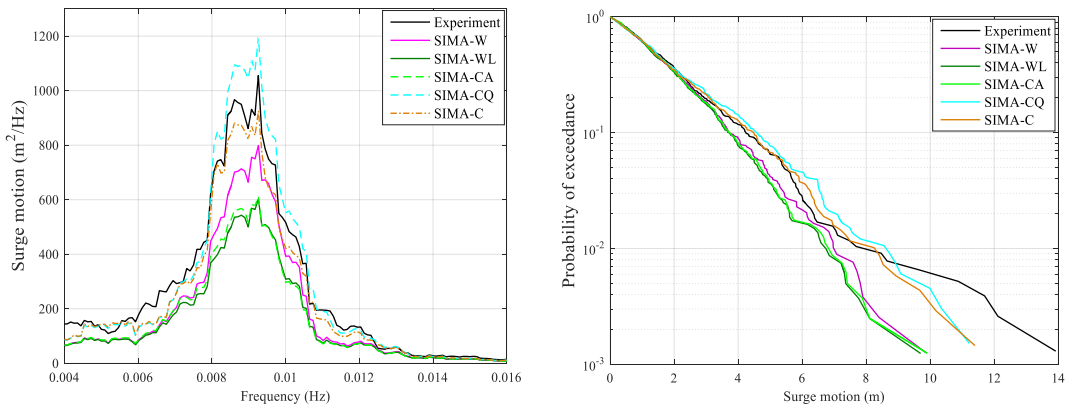
**Fig. 12.** Surge motion in the OC6 project (left: PSD, right: probability of exceedance of all local maxima and minima).

**Table 7**
Statistical results and PSD sums for surge motion in the OC6 project.

|  | Mean (m) | Diff. (%) | Standard deviation (m) | Diff. (%) | Surge PSD sum (m²) | Diff. (%) | Wave PSD sum (m²) | Diff. (%) |
|---|---|---|---|---|---|---|---|---|
| Experiment | 1.397 | 0 | 2.156 | 0 | 2.75 | 0 | 0.763 | 0 |
| SIMA-W | 1.329 | 4.87 | 1.858 | 13.82 | 1.995 | 27.45 | 0.686 | 10.09 |
| SIMA-WL | 1.323 | 5.30 | 1.745 | 19.06 | 1.605 | 41.64 | 0.686 | 10.09 |
| SIMA-CA | 1.326 | 5.08 | 1.768 | 18.00 | 1.655 | 39.82 | 0.699 | 8.39 |
| SIMA-CQ | 1.472 | 5.34 | 2.138 | 0.83 | 2.922 | 6.25 | 0.695 | 8.91 |
| SIMA-C | 1.468 | 5.08 | 2.019 | 6.35 | 2.419 | 12.04 | 0.708 | 7.21 |

for the surge motion in Fig. 13. The solid line shows a fitted Gumbel distribution while the maxima from each simulation with different wave seeds are shown as markers. For all SIMA models, the numerical data are well-described by the Gumbel function. Generally, the predicted maxima for an exceedance level of 90% in the model with modified surge force QTF increases by 9.3% compared to the result from potential flow solutions, while the modified damping reduces the predicted maxima by up to 3.5%.

Fig. 14 and Table 8 compare the heave motions between the experiment and all SIMA models. Like heave decay, in SIMA-C model, the difference-frequency heave force QTF is not modified, considering the minor effect on the motions and relatively high heave resonance frequency (which is likely to be excited by first-order waves). Heave resonance contributes equally as the wave frequency component to the total heave motion. Better agreement between the experimental and numerical results occurs in the wave-frequency region. The potential flow solution (SIMA-W) significantly overestimates the heave resonance due to the lack of low-frequency damping. The overestimation of heave resonance reduces by almost 50% with consideration of the additional linear damping (SIMA-WL) or the modified frequency-dependent damping (SIMA-C). However, the low-frequency damping has minor influence on the local maxima and standard deviation of heave motion (within 6%). Additionally, the heave resonance frequencies in the numerical results slightly deviate from the measured frequency, and the frequency in SIMA-C with larger added mass shifts towards the
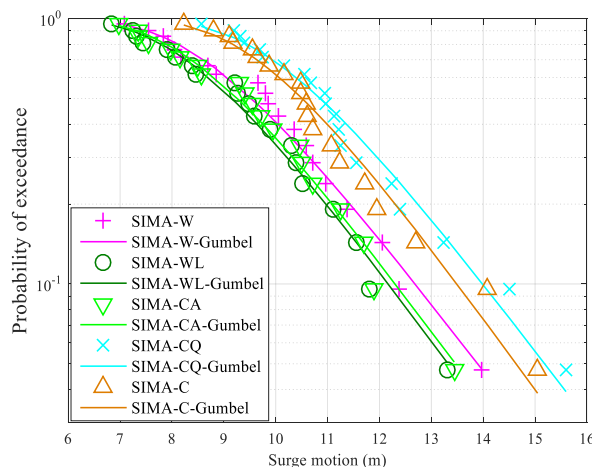


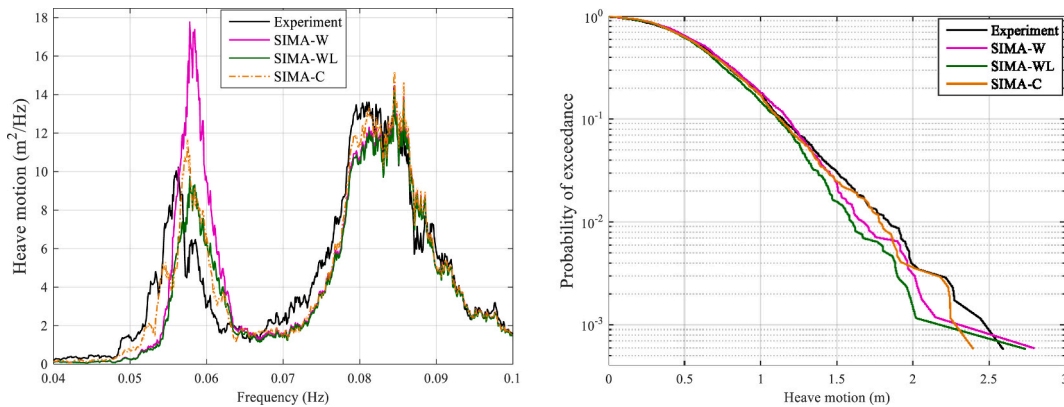**Fig. 13.** Three-hour maximum surge motion in the OC6 project.

**Fig. 14.** Heave motion in the OC6 project (left: PSD, right: probability of exceedance of all local maxima and minima).

**Table 8**
Statistical results and PSD sums for heave motion in the OC6 project.

|  | Mean (m) | Diff. (%) | Standard deviation (m) | Diff. (%) | Heave PSD sum (m²) | Diff. (%) | Wave PSD sum (m²) | Diff. (%) |
|---|---|---|---|---|---|---|---|---|
| Experiment | 0.035 | 0 | 0.543 | 0 | 0.040 | 0 | 0.171 | 0 |
| SIMA-W | 0.046 | 23.91 | 0.541 | 0.37 | 0.060 | 50.0 | 0.156 | 8.77 |
| SIMA-WL | 0.046 | 23.91 | 0.510 | 6.08 | 0.036 | 10.0 | 0.153 | 10.53 |
| SIMA-C | 0.031 | 11.42 | 0.531 | 2.21 | 0.043 | 7.5 | 0.163 | 4.68 |

experimental result. There are two possible explanations: one is the uncertainty of mooring stiffness (about 10%) in the experiment [42], another is the underestimation of the added mass in the numerical models. The mean heave motions are close to zero, which leads to a large apparent relative variation among different numerical models. Among all numerical models, SIMA-C performs best in simulating the heave motions both in the heave resonant frequency and wave frequency range.

Fig. 15 compare the 3-h maximum heave motions in different SIMA models. Due to the lack of low-frequency damping, SIMA-W predicts the largest maxima for a given exceedance probability, while the predicted maxima in SIMA-WL and SIMA-C are close to each other. The Gumbel function fits well for most of the original maximum values, but differs in larger values due to the outliers over 2.8 m. These outliers are related to the same large wave events as in Fig. 11.

The pitch motions are compared in Fig. 16 and Table 9. The main contribution to pitch motions comes from the pitch resonance, shown in the left subplot of Fig. 16. The wave-frequency response is relatively small. There is also a small response around the surge natural frequency due to coupling between pitch and surge motions, which is also compared in the PSD sums of Table 9.

The numerically estimated pitch resonant frequency is overpredicted by about 6% compared to the measured frequency. The uncertainty in the vertical center of mass (0.21 m) [42] contributes significantly to the uncertainty of the pitch resonance frequency (about 3%). The response at the pitch resonance frequency is mainly affected by the difference-frequency pitch moment QTF, which increases when modified based on CFD simulations. There is a corresponding increase in the maxima and in the standard deviation of pitch motion in SIMA-CQ and SIMA-C.

Fig. 16 shows that the SIMA-CQ and SIMA-C models each have one very large extreme value (close to 9 deg), which corresponds to a particularly large wave event at around 3230 s, as shown in Fig. 17. The reason for this overprediction may be related to the highly nonlinear wave elevation (left subplot of Fig. 17), which is treated as a linear input in SIMA. The modification of the QTF results in a changes in the phase of the second order force. For this event, the difference-frequency pitch excitation has an additive phasing effect for the modified QTF, while the original QTF results in a subtractive phasing effect.

The nearly identical pitch resonant frequency in the numerical results illustrates that the effect of changed added mass on the pitch resonant frequency is negligible. The larger damping in SIMA-CA or SIMA-WL reduces the pitch resonance and standard deviation of pitch motion, but has limited influence on the maxima. The mean value and wave frequency responses can be captured well in all SIMA models. The combination of the modified pitch moment QTF and added mass and damping gives the best agreement with the experiment for the low-frequency pitch motion.

The 3-h maximum pitch motions are compared in Fig. 18. The maxima of pitch motion over an exceedance level of 90% increases by over 35% with the modified difference-frequency pitch moment QTF. The effect of low-frequency damping is less significant. In addition, all maxima in the models with modified QTFs (SIMA-CQ, SIMA-C) fit with Gumbel function well, while larger differences can be found in the other three SIMA models due to the outliers (around 6.5 deg) which correspond to the realizations with largest maximum wave elevation (8.35 m in Fig. 11).

### 4.2.2. Mooring line tension

Considering symmetry, the mooring line tension on the starboard side (Mooring line 2, right subplot of Fig. 1) should be equal to the
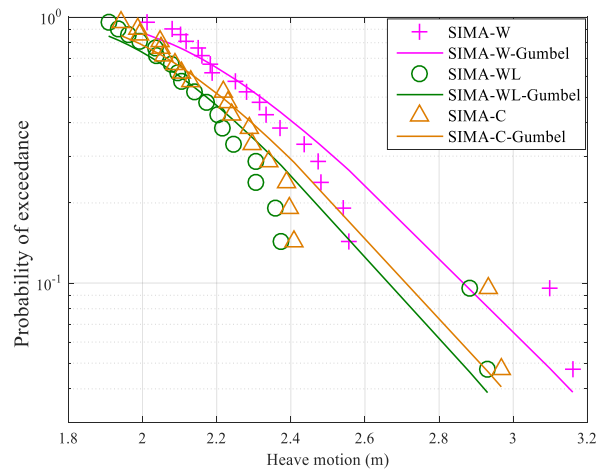
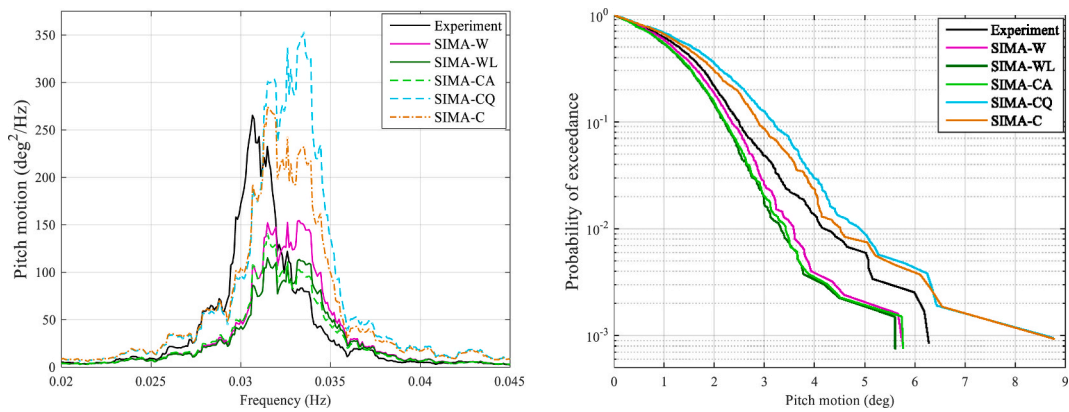**Fig. 15.** Three-hour maximum heave motion in the OC6 project.



**Fig. 16.** Pitch motion in the OC6 project (left: wave spectra, right: probability of exceedance of all local maxima and minima).

**Table 9**
Statistical results and PSD sums for pitch motion in the OC6 project.

| | Mean (deg) | Diff. (%) | Standard deviation (deg) | Diff. (%) | Surge PSD sum (deg$^2$) | Diff. (%) | Pitch PSD sum (deg$^2$) | Diff. (%) | Wave PSD sum (deg$^2$) | Diff. (%) |
|---|---|---|---|---|---|---|---|---|---|---|
| Experiment | 0.060 | 0 | 1.22 | 0 | 0.020 | 0 | 0.768 | 0 | 0.251 | 0 |
| SIMA-W | 0.057 | 5.0 | 1.11 | 9.02 | 0.004 | 80.0 | 0.595 | 22.53 | 0.237 | 5.58 |
| SIMA-WL | 0.057 | 5.0 | 1.04 | 14.75 | 0.004 | 80.0 | 0.460 | 40.10 | 0.237 | 5.58 |
| SIMA-CA | 0.056 | 6.67 | 1.05 | 13.93 | 0.005 | 75.0 | 0.487 | 36.59 | 0.238 | 5.18 |
| SIMA-CQ | 0.062 | 3.33 | 1.49 | 22.13 | 0.015 | 25.0 | 1.281 | 66.80 | 0.225 | 10.36 |
| SIMA-C | 0.061 | 1.67 | 1.38 | 13.11 | 0.016 | 20.0 | 1.026 | 33.59 | 0.227 | 9.56 |

tension on the port side (Mooring line 3, right subplot of Fig. 1). Therefore, only the tension of mooring line 1 and 2 (ML1 and ML2) are presented in this section. In addition, the pretension is subtracted from presented results. The mooring line tension is compared for the linear mooring system with 3 taut-spring-lines that was used in the OC6 project.

The upwind mooring line (ML1) tension is shown in Fig. 19 and Table 10. The largest contribution to the ML1 tension comes from the surge natural frequency (as shown in the left subplot of Fig. 19), while two smaller peaks are observed at the pitch natural frequency and wave frequency. Similar to surge motion, the tension around the surge natural frequency increases by about 45% in the models with the modified difference-frequency QTFs (SIMA-CQ, SIMA-C) and decreases in the model with the modified damping (SIMA-CA) or the additional damping (SIMA-WL). The effects of modifying the added mass are not significant. The maximum tension increases by around 15% when the modified QTFs are used, but no obvious difference is found for different levels of damping. All numerical models overestimate the wave-frequency responses by over 20%. The uncertainty of wave-frequency PSD sum is about 20% due to the uncertainty of mooring line axial stiffness (10%) in the experiment [42]. From the comparisons, SIMA-C with modified QTFs
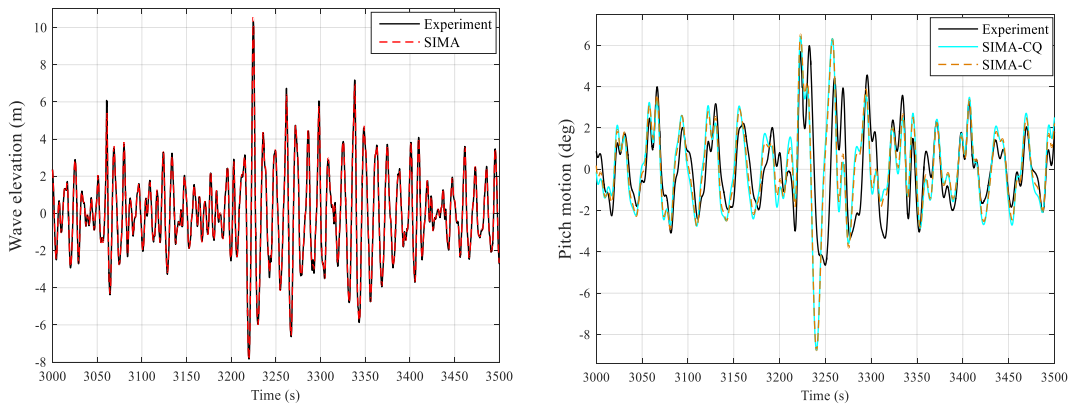
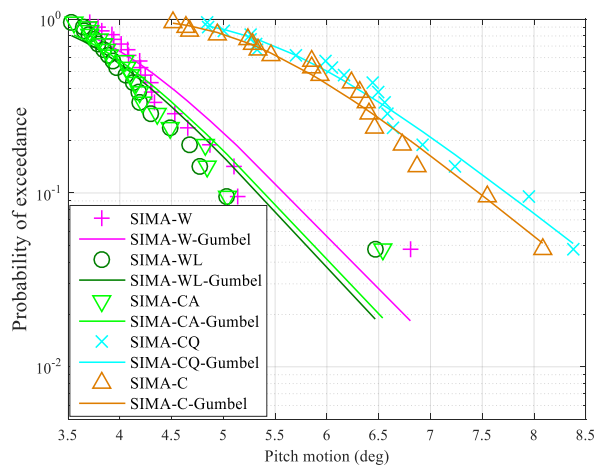**Fig. 17.** Time series of wave elevation (left) and pitch motion (right) in the OC6 project.



**Fig. 18.** Three-hour maximum pitch motion in the OC6 project.
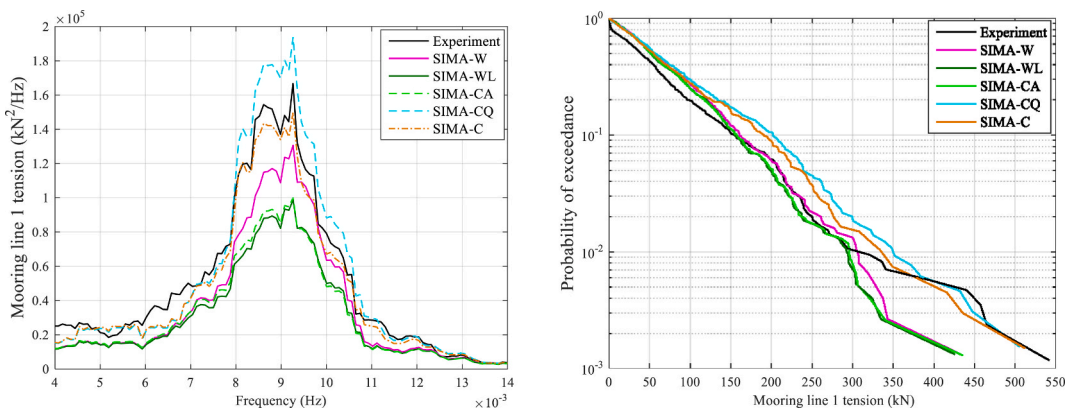


**Fig. 19.** Mooring line tension for ML1 in the OC6 project (left: PSD, right: probability of exceedance of all local maxima and minima).

and added mass and damping captures the upwind mooring line tension best.

The 3-h maximum tensions of the upwind mooring line (ML1) are shown in Fig. 20. As for surge, the Gumbel function fits with the numerical data well in all SIMA models. The model with modified QTFs predicts about 15% larger maxima than the model with potential flow solutions for an exceedance level of 90%, while the modified damping has a smaller influence on the predicted maxima.

Similar to the upwind mooring line (ML1), the tensions of mooring line on the starboard side (ML2) are dominated by responses

**Table 10**
Statistical results and PSD sums for mooring line tension of ML1 in the OC6 project (after subtracting pretension).

|  | Mean (kN) | Diff. (%) | Standard deviation (kN) | Diff. (%) | Surge PSD sum (kN$^2$) | Diff. (%) | Pitch PSD sum (kN$^2$) | Diff. (%) | Wave PSD sum (kN$^2$) | Diff. (%) |
|---|---|---|---|---|---|---|---|---|---|---|
| Experiment | 55.51 | 0 | 84.87 | 0 | 4338 | 0 | 221.1 | 0 | 824.5 | 0 |
| SIMA-W | 56.57 | 1.91 | 76.74 | 9.58 | 3267 | 24.69 | 184.5 | 16.55 | 1024 | 24.20 |
| SIMA-WL | 56.20 | 1.24 | 71.62 | 15.61 | 2637 | 39.21 | 145.4 | 34.24 | 995.5 | 20.74 |
| SIMA-CA | 56.34 | 1.50 | 72.61 | 14.44 | 2712 | 37.48 | 156.4 | 29.26 | 1020 | 23.71 |
| SIMA-CQ | 62.58 | 12.74 | 88.27 | 4.01 | 4738 | 9.22 | 311.2 | 40.75 | 1024 | 24.20 |
| SIMA-C | 62.24 | 12.12 | 82.83 | 2.40 | 3923 | 9.57 | 246.0 | 11.23 | 1019 | 23.59 |

around the surge natural frequency which are shown in Fig. 21. A difference is that there is a smaller response around the heave natural frequency besides the pitch natural frequency and wave frequency, all of which are shown in Table 11. The modified QTFs and added mass and damping have the same effect on the tension of ML2 as on ML1, and SIMA-C is also the best model to capture the tension of ML2 compared to the experiment measurements. Due to the positive mean surge motion, the mean value of the dynamic tension of ML2 is negative. It can be noted that the 3-h maximum tension of ML2 (Fig. 22) has similar variation in different SIMA models as tension of ML1 (Fig. 20).

The damage equivalent loads for the mooring lines are shown in Fig. 23. The percentage on each bar represents the difference compared to the experimental results. The potential flow solution (SIMA-W) underestimates the damage equivalent load, and the additional damping in SIMA-WL increases this underestimation. It can be seen the damage equivalent loads are fairly consistent for models with similar damping (SIMA-WL vs SIMA-CA). The modified difference-frequency QTFs (SIMA-CQ) increase the damage equivalent load, resulting in an overestimation (4.74%). The overestimation is reduced and the best agreement with the experimental results is achieved when the QTFs, added mass and damping are modified (SIMA-C) together.

### 4.2.3. Tower base load

In this section, the experimental data are from the OC5 project. The tower bending natural frequency is about 0.32 Hz [4], which is larger than the wave frequency (0.0826 Hz) of irregular wave and can be excited by the sum-frequency wave loads. Meanwhile, the low-frequency wave loads also contribute to the tower base load for a semi-submersible FWT [4]. An example of tower base fore-aft moment ($M_y$ in Fig. 6) is shown in Fig. 24. The PSD of fore-aft moment shows three distinct frequencies: the pitch natural frequency at 0.03 Hz, the linear wave excitation around 0.14 Hz and the tower-bending natural frequency about 0.32 Hz. The motion of floater related to the irregular wave creates a larger response around 0.14 Hz occurring away from the wave peak frequency. SIMA with either sum-frequency ('SF' in Fig. 24) or difference-frequency ('DF' in Fig. 24) QTFs underestimates the low-frequency or high-frequency responses, respectively. Therefore, all SIMA models presented in this section consider both QTFs. An example (SIMA-C) is shown in Fig. 24 where both low-frequency and high-frequency responses are captured well.

The largest contribution to the stress on the leading edge of tower base (Point B in Fig. 6) comes from the fore-aft moment which is considered in Fig. 25 and Table 12. The sum-frequency QTFs from potential flow solution are implemented for all numerical models. The other settings in different SIMA models follow the descriptions in Table 3. The ranges of frequency for calculating the PSD sum are shown in Fig. 24. The wave-frequency responses are underpredicted by more than 12% (Table 12). However, all SIMA models overpredict the responses around tower-bending natural frequency by over 60% which not only depend on the potential flow solution, but also relate to the motions which are compared in Fig. 26. A larger overprediction up to 101% is seen when the difference-frequency QTF from potential flow solutions (SIMA-W, SIMA-WL, SIMA-CA) is applied. In addition, the modified difference-frequency QTFs (SIMA-CQ, SIMA-C) reduce the underprediction of low-frequency responses in the potential flow solutions (left subplot of Fig. 25) and predict larger bending moments (by about 6%) down to the probability of 0.5% (right subplot of Fig. 25). For even smaller probabilities, the models with potential flow solution (SIMA-W, SIMA-WL,SIMA-CA) predict larger moments, which depend on the high frequency responses (right subplot of Fig. 27). However, these larger values disappear in the short-term extreme value analysis (Fig. 28) when using numerically generated irregular waves. Additionally, the time when the maxima occurs (around 2940 s) in the model with potential flow solution (SIMA-W) does not cohere with the experimental data (around 710 s). Hence, it is not fair to declare that the potential flow solution has a better performance in predicting the maximum fore-aft moment, as shown in the right subplot of Fig. 25. Furthermore, the effect of low-frequency damping on the maxima is negligible.

**Table 11**
Statistical results and PSD sums for mooring line tension of ML2 in the OC6 project (after subtracting pretension).

|  | Mean (kN) | Diff (%) | Standard deviation (kN) | Diff. (%) | Surge PSD sum (kN$^2$) | Diff. (%) | Pitch PSD sum (kN$^2$) | Diff. (%) | Heave PSD sum (kN$^2$) | Diff. (%) | Wave PSD sum (kN$^2$) | Diff. (%) |
|---|---|---|---|---|---|---|---|---|---|---|---|---|
| Experiment | −27.06 | 0 | 41.90 | 0 | 1032 | 0 | 52.12 | 0 | 26.48 | 0 | 254.9 | 0 |
| SIMA-W | −24.06 | 11.1 | 37.17 | 11.3 | 735.8 | 28.7 | 56.62 | 8.64 | 32.44 | 22.5 | 273.5 | 7.30 |
| SIMA-WL | −24.07 | 11.0 | 34.88 | 16.8 | 592.2 | 42.6 | 43.06 | 17.4 | 17.17 | 35.2 | 283.5 | 11.2 |
| SIMA-CA | −27.09 | 1.11 | 35.41 | 15.5 | 609.1 | 41.0 | 46.01 | 11.7 | 18.14 | 31.5 | 293.3 | 15.1 |
| SIMA-CQ | −26.81 | 0.92 | 42.64 | 1.77 | 1052 | 1.94 | 88.32 | 69.5 | 38.76 | 46.4 | 287.1 | 12.6 |
| SIMA-C | −26.89 | 0.63 | 40.21 | 4.03 | 866.5 | 16.0 | 70.51 | 35.3 | 23.34 | 11.9 | 307.4 | 20.6 |
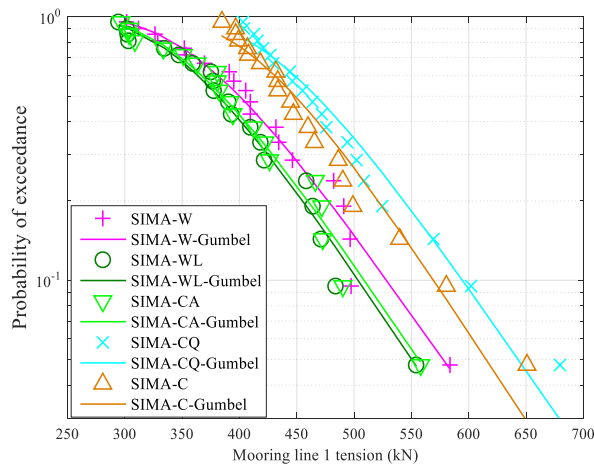
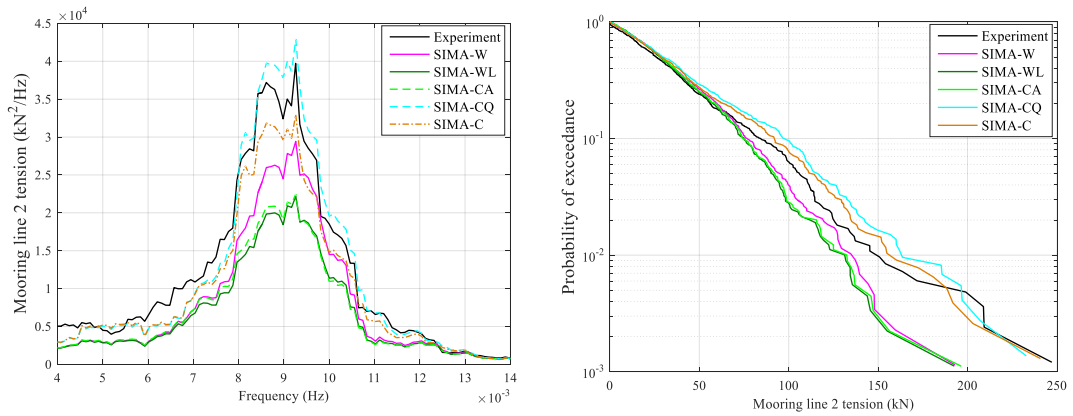**Fig. 20.** Three-hour maximum mooring line tension of ML1 in the OC6 project.



**Fig. 21.** Mooring line tension for ML2 in the OC6 project (left: PSD, right: probability of exceedance of all local maxima and minima).
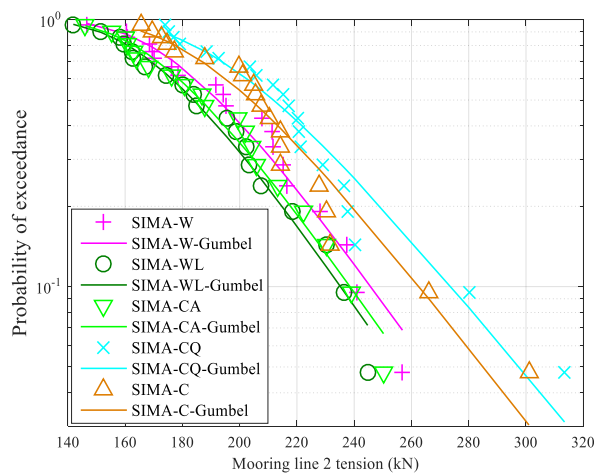


**Fig. 22.** Three-hour maximum mooring line tension of ML2 in the OC6 project.

The 3-h maxima for the tower base fore-aft bending moment are compared in Fig. 26. The effect of modified difference-frequency QTFs is dominant and increases the maxima over an exceedance level of 90% by 8.5%. The modified damping has minor influence. The damage equivalent loads for the tower base are shown in Fig. 29 with the difference compared to the experimental results.
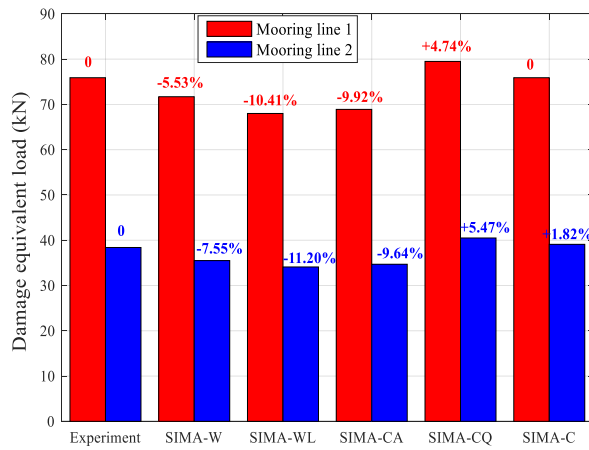
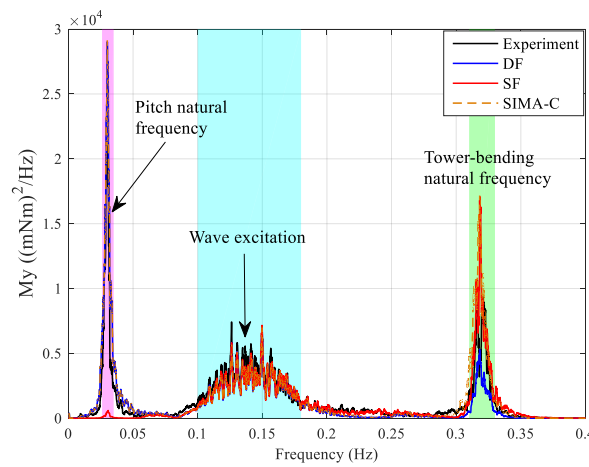**Fig. 23.** Damage equivalent loads for mooring line 1 and 2 in the OC6 project.



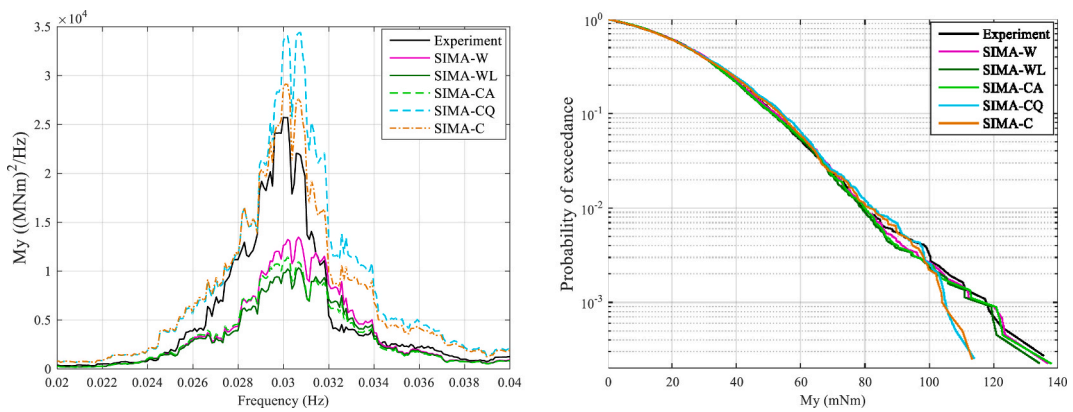**Fig. 24.** PSD of the tower base fore-aft moment in the OC5 project.



**Fig. 25.** Tower base fore-aft moment in the OC5 project (left: PSD, right: probability of exceedance of all local maxima and minima).

**Table 12**
Statistical results and PSD sums for tower base fore-aft moment in the OC5 project.

| | Mean (kNm) | Diff. (%) | Standard deviation (kNm) | Diff. (%) | Pitch PSD sum (mNm²) | Diff. (%) | Wave PSD sum (mNm²) | Diff. (%) | Tower bending PSD sum (mNm²) | Diff. (%) |
|---|---|---|---|---|---|---|---|---|---|---|
| Experiment | −495.1 | 0 | 2345 | 0 | 81.29 | 0 | 246.0 | 0 | 89.04 | 0 |
| SIMA-W | −415.3 | 16.1 | 2354 | 0.38 | 53.17 | 52.9 | 216.0 | 12.19 | 179.1 | 101 |
| SIMA-WL | −415.3 | 16.1 | 2310 | 1.49 | 43.28 | 46.8 | 215.7 | 12.32 | 170.5 | 90.9 |
| SIMA-CA | −423.2 | 14.5 | 2326 | 0.81 | 45.99 | 43.4 | 214.8 | 12.68 | 175.8 | 97.4 |
| SIMA-CQ | −489.2 | 1.19 | 2490 | 6.18 | 118.2 | 42.4 | 211.6 | 13.98 | 146.8 | 64.9 |
| SIMA-C | −496.0 | 0.18 | 2443 | 4.18 | 101.6 | 24.9 | 210.6 | 14.39 | 145.0 | 62.8 |
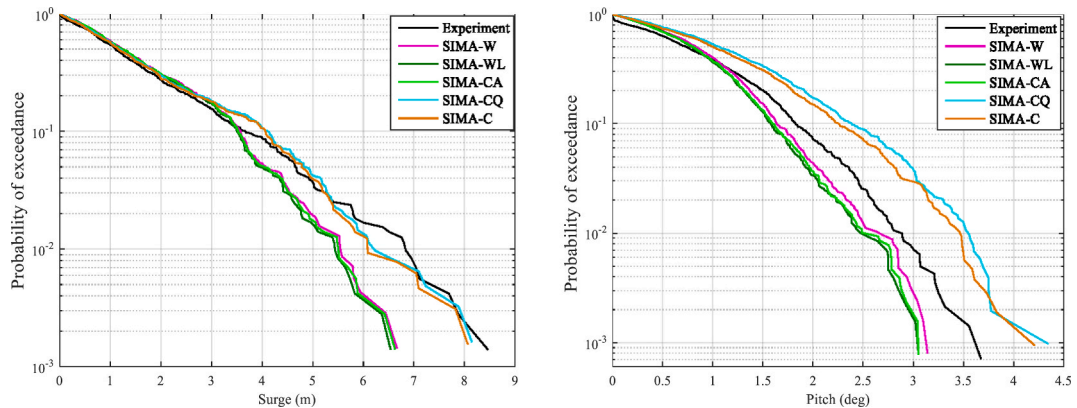


**Fig. 26.** Probability of exceedance for surge (left) and pitch (right) motions in the OC5 project.
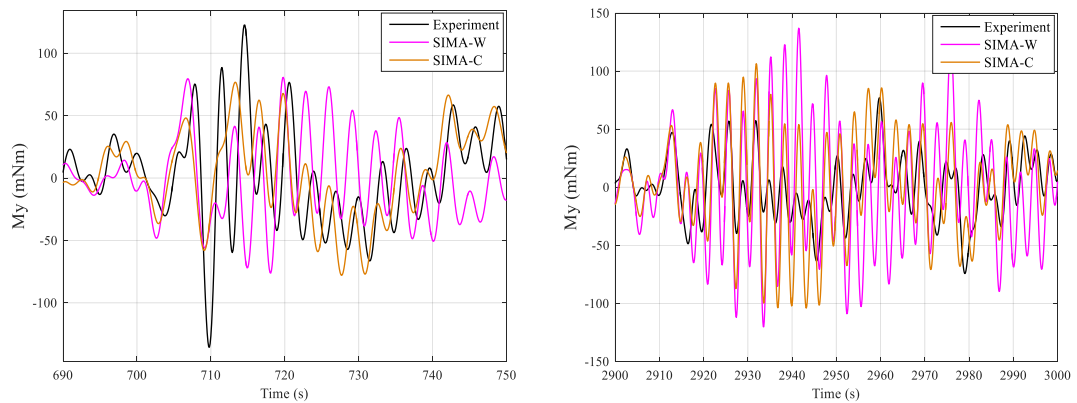


**Fig. 27.** Different time series of tower base fore-aft moment in the OC5 project.

Different SIMA models predict similar wave-frequency responses, but differ in estimating the low- and high-frequency responses. Considering the longer period for the low-frequency responses, the effect on the fatigue is limited. Even so, the more low-frequency responses the model can capture, the better agreement the estimated damage equivalent load is with the experimental data. This is consistent with the finding in the OC5 project that the tower base loads around pitch natural frequency have an significant effect on the damage-equivalent load [4].

## 5. Conclusions

This study investigates the dynamic responses of a semi-submersible FWT based on modifying the difference-frequency QTF and frequency-dependent added mass and damping from potential flow theory using CFD simulations. Decay tests in still water and irregular wave tests are considered to compare the numerically estimated results against experimentally measured data.

The QTF values estimated by the difference-frequency forces on a restrained FWT in the CFD simulations have been corrected for the floating condition based on the assumption that the contributions of the first-order motion can be accurately estimated in the potential flow theory. The modified QTFs have larger magnitudes, especially at higher wave frequencies. The frequency-dependent
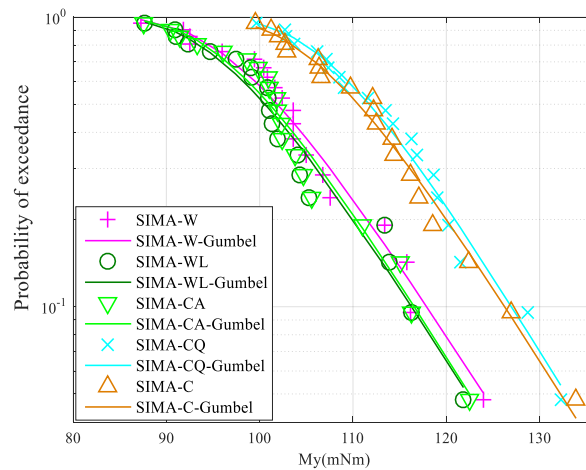
**Fig. 28.** Three-hour maxiamum tower base fore-aft moment in the OC5 project.
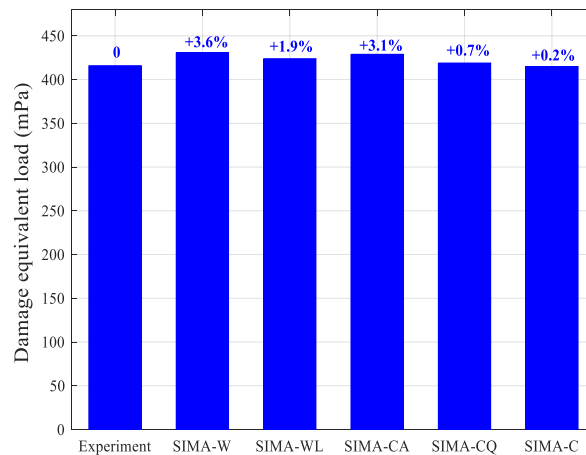


**Fig. 29.** Damage equivalent load for the leading edge (Point B in Fig. 5) of tower base in the OC5 project.

added mass and damping are modified by the estimated added mass and linearized damping from forced oscillation tests in the CFD simulations. The potential flow theory underestimates the amplitude of added mass by over 10%. The quadratic damping in Morison drag force also underestimates the nonlinear viscous damping. This depends on the selected drag coefficients.

In the free decay tests, there is no effect of modified difference-frequency QTFs. After modifying the frequency-dependent added mass and damping based on the CFD forced oscillation simulations, the underestimation of damping in the potential flow solution reduces and the engineering tool can capture similar damping as the CFD model. Although there are differences in the added mass and damping, the predicted natural periods in all numerical models are close to the experimental results (within 5%).

The natural frequencies of the floater motions are outside the linear wave-excitation range, and must be excited by some nonlinear forces. The largest contribution to the motions comes from the resonant frequency, except for the heave motion with equal contributions from the resonant and wave frequencies. The difference-frequency QTFs from the potential flow theory result in underestimation of the responses at resonant frequencies. The additional linear damping for matching calculated free decay motions from the CFD simulations increases this underestimation. However, when the difference-frequency QTFs are modified based on CFD simulations with a restrained floater, the motions are overestimated compared to the experimental data. The overestimation can be reduced by adjusting the frequency-dependent damping at the same time. There is a good agreement between experiment and engineering tools with modified QTFs and added mass and damping. The same trend is also valid for the exceedance probability distribution, standard deviation and extreme values of motions.

Considering symmetry, only the tensions of upwind mooring line and mooring line on the starboard side are investigated. The tension is mainly influenced by the surge resonance. Therefore, the difference-frequency QTFs and added mass and damping influence the tension in the same way as the surge motion. The damage-equivalent tension in the mooring line increases when more difference-frequency wave loads are captured and decreases with increasing damping.

For the tower base fore-aft moment, there are three significant contributions: the pitch natural frequency, wave frequency and

tower bending natural frequency. The modified hydrodynamics from the CFD simulations influence the responses around pitch natural frequency and tower bending natural frequency. Although the low-frequency moments have a longer period, the more low-frequency responses the model can capture, the better agreement the estimated damage equivalent load of tower base is with the experimental data.

In conclusion, more accurate estimation of nonlinear hydrodynamics on the floater in the CFD simulations reduces the under-prediction of the low-frequency dynamic responses of a semi-submersible FWT in the potential flow solutions and show the best agreement with the experimental measurements.

## Declaration of competing interest

The authors declare that they have no known competing financial interests or personal relationships that could have appeared to influence the work reported in this paper.

## Acknowledgements

## References

[1] Cordle A, Jonkman J. National renewable energy lab. (NREL), golden, CO (United States). State of the art in floating wind turbine design tools 2011.
[2] Coulling AJ, et al. Importance of second-order difference-frequency wave-diffraction forces in the validation of a FAST semi-submersible floating wind turbine model. No. NREL/CP-5000-57697. ASME 2013 32nd International Conference on Ocean, Offshore and Arctic Engineering 2013 [American Society of Mechanical Engineers Digital Collection].
[3] Mercier JA, Leverette SJ, Bliault AL. Evaluation of Hutton TLP response to environmental loads. Offshore technology conference 1982 [Offshore Technology Conference].
[4] Robertson AN, et al. OC5 project phase II: validation of global loads of the DeepCwind floating semisubmersible wind turbine. Energy Procedia 2017;137:38–57.
[5] Wei Y-f, Yang J-m, Chen X. A Review of the hydrodynamic Performance of heave damping Plates on spar platform [J]. China Offshore Platform 2010:6.
[6] Robertson A, et al. National renewable energy lab. (NREL), golden, CO (United States). Definition of the semisubmersible floating system for phase II of OC4. No. NREL/TP-5000-60601 2014.
[7] Robertson A, et al. Technical report NREL. Definition of the OC5 DeepCwind semisubmersible floating system 2016.
[8] Bayati I, et al. The effects of second-order hydrodynamics on a semisubmersible floating offshore wind turbine. J Phys Conf 2014 [IOP Publishing].
[9] Cao Q, et al. Second-order responses of a conceptual semi-submersible 10 MW wind turbine using full quadratic transfer functions. Renew Energy 2020;153: 653–68.
[10] Gueydon S, Duarte T, Jonkman J. Comparison of second-order loads on a semisubmersible floating wind turbine. Int Conf Offshore Mech Arctic Eng 2014 [American Society of Mechanical Engineers].
[11] Kvittem MI, Bachynski EE, Moan T. Effects of hydrodynamic modelling in fully coupled simulations of a semi-submersible wind turbine. Energy Procedia 2012; 24:351–62.
[12] Zhang L, et al. Second-order hydrodynamic effects on the response of three semisubmersible floating offshore wind turbines. Ocean Eng 2020;207:107371.
[13] Xu K, Gao Z, Moan T. Effect of hydrodynamic load modelling on the response of floating wind turbines and its mooring system in small water depths. J Phys Conf 2018 [IOP Publishing].
[14] Luan C, Gao Z, Moan T. Design and analysis of a braceless steel 5-MW semi-submersible wind turbine. ASME 2016 35th International Conference on Ocean, Offshore and Arctic Engineering 2016 [American Society of Mechanical Engineers Digital Collection].
[15] Wang L, et al. Uncertainty assessment of CFD investigation of the nonlinear difference-frequency wave loads on a semisubmersible FOWT platform. Sustainability 2021;13(1):64.
[16] Benitz MA, et al. Comparison of hydrodynamic load predictions between reduced order engineering models and computational fluid dynamics for the OC4-DeepCwind semi-submersible. No. NREL/CP-5000-61157. ASME 2014 33rd International Conference on Ocean, Offshore and Arctic Engineering 2014 [American Society of Mechanical Engineers Digital Collection].
[17] Benitz MA, et al. Validation of hydrodynamic load models using CFD for the OC4-DeepCwind semisubmersible. No. NREL/CP-5000-63751. ASME 2015 34th International Conference on Ocean, Offshore and Arctic Engineering 2015 [American Society of Mechanical Engineers Digital Collection].
[18] Lopez-Pavon C, Souto-Iglesias A. Hydrodynamic coefficients and pressure loads on heave plates for semi-submersible floating offshore wind turbines: a comparative analysis using large scale models. Renew Energy 2015;81:864–81.
[19] Bozonnet P, Emery A. International society of offshore and polar engineers. CFD simulations for the design of offshore floating wind platforms encompassing heave plates. in The Twenty-fifth International Ocean and Polar Engineering Conference 2015.
[20] Burmester S, et al. Investigation of a semi-submersible floating wind turbine in surge decay using CFD. Ship Technol Res 2020;67(1):2–14.
[21] Wang Y, et al. CFD simulation of semi-submersible floating offshore wind turbine under pitch decay motion. Int Conf Offshore Mech Arctic Eng 2019 [American Society of Mechanical Engineers].
[22] Bruinsma N, Paulsen B, Jacobsen N. Validation and application of a fully nonlinear numerical wave tank for simulating floating offshore wind turbines. Ocean Eng 2018;147:647–58.
[23] Rivera-Arreba I, et al. Modeling of a semisubmersible floating offshore wind platform in severe waves. J Offshore Mech Arctic Eng 2019;141:6.
[24] Tran TT, Kim D-H. The coupled dynamic response computation for a semi-submersible platform of floating offshore wind turbine. Journal of wind engineering and industrial aerodynamics 2015;147:104–19.
[25] Wang Y, et al. CFD simulation of semi-submersible floating offshore wind turbine under regular waves. The 30th International Ocean and Polar Engineering Conference 2020 [International Society of Offshore and Polar Engineers].
[26] Robertson A, et al. OC6 Phase I: investigating the underprediction of low-frequency hydrodynamic loads and responses of a floating wind turbine. TORQUE 2020;2020.
[27] Weller HG, et al. A tensorial approach to computational continuum mechanics using object-oriented techniques. Computers in physics 1998;12(6):620–31.
[28] Hirt CW, Nichols BD. Volume of fluid (VOF) method for the dynamics of free boundaries. Journal of computational physics 1981;39(1):201–25.
[29] Li H, Bachynski-Polić EE. Experimental and numerically obtained low-frequency radiation characteristics of the OC5-DeepCwind semisubmersible. Ocean Eng 2021;232:109130.

[30] Li H. Analysis of difference-frequency wave loads and quadratic transfer functions on a restrained semi-submersible floating wind turbine. Ocean Eng 2021;232: 109165.

[31] Marintek, Simo—Theory Manual Version 4.0. Marintek trondheim, Norway. 2012.

[32] Ormberg H, Passano E. *RIFLEX theory manual.* Marintek. Trondheim 2012.

[33] Lee C-H. Massachusetts Institute of technology, department of ocean engineering. WAMIT theory manual 1995.

[34] Cummins W. The impulse response function and ship motions. 1962 [David Taylor Model Basin Washington DC].

[35] Tom N, et al. Bichromatic wave selection for validation of the difference-frequency transfer function for the OC6 validation campaign. Int Conf Offshore Mech Arctic Eng 2019 [American Society of Mechanical Engineers].

[36] Pinkster JA. Low frequency second order wave exciting forces on floating structures. 1980.

[37] Kvittem MI, Moan T. Time domain analysis procedures for fatigue assessment of a semi-submersible wind turbine. Mar Struct 2015;40:38–59.

[38] Li H, et al. Short-term fatigue analysis for tower base of a spar-type wind turbine under stochastic wind-wave loads. International Journal of Naval Architecture and Ocean Engineering 2018;10(1):9–20.

[39] Hayman G. National renewable energy laboratory (NREL). 2012.

[40] Matsuishi M, Endo T. Fatigue of metals subjected to varying stress. Japan Society of Mechanical Engineers. Fukuoka, Japan 1968;68(2):37–40.

[41] Naess A, Moan T. Stochastic dynamics of marine structures. Cambridge University Press; 2013.

[42] Robertson A, et al. Total experimental uncertainty in hydrodynamic testing of a semisubmersible wind turbine, considering numerical propagation of systematic uncertainty. Ocean Eng 2020;195:106605.

[43] Robertson AN. Uncertainty analysis of OC5-DeepCwind floating semisubmersible offshore wind test campaign. NREL/CP-5000-68035. National Renewable Energy Lab. (NREL), Golden, CO (United States) 2017.